Magnon gap mediated lattice thermal conductivity in $MnBi_2Te_4$

Dung D. Vu[1,†], Ryan A. Nelson[4,‡], Brandi L. Wooten[3,§], Joseph Barker[5,‖], Joshua E. Goldberger[4,¶], Joseph P. Heremans[1,2,3,#,*]

[1] Department of Mechanical and Aerospace Engineering, The Ohio State University, Columbus, OH 43210, USA.
[2]Department of Physics, The Ohio State University, Columbus, OH 43210, USA.
[3]Department of Materials Science and Engineering, The Ohio State University, Columbus, OH 43210, USA.
[4]Department of Chemistry and Biochemistry, The Ohio State University, Columbus, OH 43210, USA.
[5]School of Physics and Astronomy, University of Leeds, United Kingdom.
* Corresponding author (Email: heremans.1@osu.edu)
[†]ORCID 0000-0001-9085-0436
[‡]ORCID 0000-0003-0763-1094
[§]ORCID 0000-0003-4342-5976
[‖]ORCID 0000-0003-4843-5516
[¶]ORCID 0000-0003-4284-604X
[#]ORCID 0000-0003-3996-2744

Abstract

In magnetic materials with strong spin-lattice coupling, magnon-phonon interactions can change the sensitivity of the lattice thermal conductivity in an applied magnetic field. Using an out-of-plane applied field to change $MnBi_2Te_4$ between antiferromagnetic (AFM), canted (CAFM) and ferromagnetic (FM) phases, we controlled the lattice thermal conductivity, generating both a positive and a negative magnetic field dependence. The in-plane thermal conductivity decreases with field in the AFM phase, remains approximately constant in the CAFM phase, and increases with field in the FM phase. We explain this in terms of the field-induced changes of the magnon gap which modifies magnon-phonon scattering. We also report thermal Hall data measured in the same configuration.

Introduction

The thermal conductivity of a solid has contributions from phonons, electrons and magnons. The thermal conductivity of the electrons can be modulated in a magnetic field via the Lorentz force, giving rise to magnetoresistance, which is a negative magneto-thermal conductivity, or the recently discovered thermal chiral anomaly which gives a positive magneto-thermal conductivity [1]. Magnons couple directly to magnetic fields and the thermal conductivity can be altered by the Zeeman effect, red- or blue-shifting the magnon dispersion, which alters the thermal occupation of magnon states. Phonons by themselves are not generally considered to be directly affected by a magnetic field. However, in magnetic materials with strong spin-lattice coupling, magnon-phonon interactions can thoroughly change that picture. Understanding these interactions can open ways to control the lattice thermal conductivity in active thermal devices (e.g. heat switches) with a magnetic field.

$MnBi_2Te_4$, a magnetic topological insulator, crystalizes in the space group $R\bar{3}m$. It consists of septuple van der Waals layers of Te-Bi-Te-Mn-Te-Bi-Te. This creates a structure that integrates a central layer of MnTe octahedra inside the Bi_2Te_3 archetype, making it a magnetic relative of the 3D topological insulator Bi_2Te_3. $MnBi_2Te_4$ has an A-type antiferromagnetic (AFM) structure: the Mn^{2+} spins have moments that are aligned in the out-of-plane direction, are ferromagnetically coupled within each layer, but are weakly antiferromagnetically coupled with neighboring layers. The Néel temperature is $T_N = 25$ K [2]. In an out-of-plane magnetic field with temperatures below T_N, the bulk magnetic ordering undergoes a spin-flop transition followed by a canted AFM (CAFM) ordering. Further increasing the field leads to a phase where the spins in all layers align, making $MnBi_2Te_4$ appear ferromagnetic (FM) at high field [2,3] (depicted in Fig 1(a)). Theory predicts that interplay between the magnetic structure and the topologically nontrivial bands produces rich topological phase transitions in an applied magnetic field [4–7]. Raman spectroscopy studies in $MnBi_2Te_4$ show strong coupling between spin and lattice. In these studies, certain A_{1g} optical phonon modes have peak intensity strongly affected by the magnetic ordering [8,9]. Therefore, we expect magnetic ordering transitions in $MnBi_2Te_4$ to exhibit nonmonotonic magneto-electrothermal transport phenomena.

In this study we measure the in-plane thermal conductivity (κ_{xx}) of AFM-$MnBi_2Te_4$ from 2 K to 30 K in an out-of-plane magnetic field. Characteristic changes in κ_{xx} coincide with the boundaries of the field-induced magnetic phase transitions in this material. κ_{xx} decreases with field in the AFM phase, has relatively small field dependence in the canted phase, and increases again with field in the FM phase (Fig. 1(a)). The measured data agrees with reported thermal transport data in literature [10,11]. The magnitude and sign of the changes cannot be explained by either the magnon thermal conductivity or the electronic thermal conductivity. We interpret our results in terms of a magnon-number non-conserving magnon-phonon confluence interaction process. We propose that the magnon gap plays a crucial role in controlling the phase space of energy-momentum that allows magnon-phonon scattering [12], suggesting that two magnon to one phonon scattering is the dominant spin and lattice interaction in $MnBi_2Te_4$. Theoretical and experimental studies have suggested a thermal Hall effect originating from magnon-phonon interactions [13–20]. We also report thermal Hall data measured in the same configuration. Our measured thermal Hall signal is dominated by electronic thermal Hall contributions, which show an anomalous thermal Hall effect at the spin-flop transition which strongly resembles the electrical Hall data. The magnitude of the thermal Hall signal is close to an estimation using the

Wiedemann Franz Law. The result points toward an electronic origin of thermal Hall signal and shows no evidence for a thermal Hall signal originated from magnon-phonon interaction.

In-plane thermal conductivity in an out-of-plane magnetic field

Single crystals of $MnBi_2Te_4$ were grown by adapting the previously established flux method [21] by slow cooling Bi_2Te_3 and MnTe powders in approximately a 5:1 ratio into an alumina Canfield crucible and centrifuging at 595 °C. Crystals with lengths and widths of 3-8 mm and thicknesses of 10 – 200 μm were prepared for transport measurements. Hall effect characterization of the carrier concentration (see Supplemental Material) of the samples shows that electrons are the majority charge carriers. The electron concentration at 20K is about $6 \cdot 10^{19}$ - $1 \cdot 10^{20}$ cm^{-3}. This is very similar to other values reported, typically ranging from $7 \cdot 10^{19}$ - $1 \cdot 10^{20}$ cm^{-3} [22,23]. The carrier concentration indicates that the Fermi level is about 0.3 eV into the conduction band [4]. The n-type defects responsible for doping were explored by Hou *et al.* and Du *et al.* both experimentally and computationally [24,25]. $MnBi_2Te_4$ growth faces challenges with donor Bi_{Mn}+ anti-site defects [22,26], which heavily n-type dope the crystal.

Figure 1(b) shows the temperature dependence of the in-plane thermal conductivity κ_{xx} without applied magnetic field. This agrees with data previously reported in the literature [10,21]. The electronic thermal conductivity was reported to follow a T^1 law [21], and can be estimated from the resistivity of the sample using the Wiedemann-Franz law with the free-electron Lorenz ratio to be of the order of 0.2 W m^{-1} K^{-1} at 100K. It is generally much smaller than the total κ_{xx}. At temperatures slightly above 30 K, which are above the T_N of 24.5 K, the lattice thermal conductivity dominates. Around T_N and below, both the lattice thermal conductivity and the magnon thermal conductivity $\kappa_{lattice} + \kappa_{magnon}$ must be considered, while the electronic thermal conductivity diminishes and contributes less than 0.05 W m^{-1} K^{-1} to the total thermal conductivity of 2.62 W m^{-1} K^{-1}. In yttrium iron garnet (YIG), κ_{magnon} was estimated to be up to ~1 W m^{-1} K^{-1} at 2 K and becomes a significant contribution as temperature decreases [27]. If κ_{magnon}were significant in $MnBi_2Te_4$ in this range, we would see an increase of κ_{xx} as the temperature decreases below T_N, yet we observe a clear suppression of κ_{xx} in this temperature range. A similar anomaly in $\kappa_{xx}(T)$ was observed in some other magnetic materials near the ordering temperature [28–30]. Comparing the experimental data above and below the Neel temperature T_N = 24.5 K, one notices that $\kappa_{xx}(T)$ below T_N is much smaller compared to what it would be if the data above T_N were simply extrapolated following the $1/T$ law expected for the Umklapp-dominated lattice thermal conductivity. Combined with the observation of a peak in heat capacity at the Neel temperature [31], we conclude that magnons emerge at $T<T_N$ and the magnons do not carry much additional heat but instead induce strong phonon-magnon scattering in the ordered phase.

The field dependence of the in-plane thermal conductivity $\kappa_{xx}(B_z)$ is shown in Fig. 1(c-d). Note that Fig. 1(c) shows data in vicinity of T_N, while Fig. 1(d) shows data at lower temperatures. As the temperature decreases towards the ordering temperature, $\kappa_{xx}(B_z)$ develops an interesting field dependence. At 29.2K, we observe a slight increase in $\kappa_{xx}(B_z)$ with an applied magnetic field up to 9 T. This magnetic field induced increase in thermal conductivity grows larger as the temperature approaches T_N. Below T_N, 22 K < T < 25 K, κ_{xx} decreases at low field and increases linearly at high field. Far below T_N, T < 22K, the canted AFM ordering phase

appears in the intermediate field region. Our data in Fig. 1(d) shows that κ_{xx} saturates in this region with only a weak field dependence. In the FM phase, the field dependence becomes a linear increase with field. In Fig. 1(a) we plot the derivative $d\kappa_{xx} / dB_z$ as as function of B_z and T and overlay the known magnetic phase diagram [2,3]. Discontinuities in $d\kappa_{xx} / dB_z$ coincide precisely with the magnetic phase boundaries, indicating that the changes in thermal conductivity are related to the magnetic phases [2,3].

Theory for $\kappa_{xx}(B_z)$

The field dependence of the thermal conductivity below T_N is unlikely to be due to electrons, because they contribute less than 0.05 W m^{-1} K^{-1} to κ_{xx} and the resistivity data show less than a 2% decrease in a 9 T magnetic field at 25 K. Therefore, we must look at phonon and magnon contributions. Above T_N, a high magnetic field polarizes the paramagnet into a forced, more ferromagnetically ordered state; thus, magnetic scattering of phonons is reduced. This explains well the κ_{xx} (B_z) data above T_N.

The κ_{xx} (B_z) trends below T_N can be summarized as follows: A decrease in κ_{xx} (B_z) in the AFM phase that becomes more linear at lower temperature, a sharp drop at the spin-flop transition, a relatively small field dependence in the CAMF phase, and a linear increase with field in the FM phase. Strong suppression of thermal conductivity in the AFM phase and a sharp drop at the spin-flop transition were also reported in the multiferroic materials [19] and Ni_3TeO_6 [18] although the origin was not well established. A linear increase in thermal conductivity with magnetic field was also reported in $Na_2Co_2TeO_6$ [32] and attributed to a reduction of magnon-phonon scattering. An increase in thermal conductivity at high field was observed in Bi-Sb topological insulators and attributed to the thermal chiral anomaly [1]. This occurs when an applied magnetic field is colinear with the heat flux and parallel to the Weyl point separation [1]. Although the FM phase of $MnBi_2Te_4$ is predicted to be a Type II Weyl semimetal with Weyl points separation from Γ-Z [7], in our experimental setup, the applied heat flux direction is perpendicular to the Weyl point separation, ruling out the thermal chiral anomaly. The theory of Fermi arc mediated entropy transport in Weyl semimetals [33] also predicts an increase of thermal conductance that is linear with an applied magnetic field that is perpendicular to the surfaces that host topologically protected Fermi arcs. In our experimental setup, it is possible that a small, unintentional misalignment of the out-of-plane magnetic field exists, so there may be a small in-plane magnetic field component $B_{\text{in-plane}}$ perpendicular to the arcs. However, no change was observed when the $B_{\text{in-plane}}$ component was increased intentionally by setting a small (but intentionally) misaligned angle between the applied magnetic field and the sample's out-of-plane direction (see Supplementary Materials), contrary to the theoretical prediction. In our samples, we note that the position of the Fermi level (see Methods section) of $MnBi_2Te_4$ is far (0.3 eV) from the bulk gap. Thus, the measured magneto-thermal transport behavior is unlikely to be due to topological properties.

To understand the behavior of the $\kappa_{xx}(B_z)$ data below T_N, we calculated the evolution of the magnon bands and inferred the consequences for magnon-phonon interactions. We used atomistic spin dynamics (see Supplementary Materials) based on the Heisenberg model parametrized from inelastic neutron scattering measurements of $MnBi_2Te_4$ [34]. The Hamiltonian is

$$\mathcal{H} = -\frac{1}{2}\sum_{\langle ij\rangle\parallel} J_{ij}\mathbf{S}_i \cdot \mathbf{S}_j - \frac{1}{2}\sum_{\langle ij\rangle\perp} \mathbf{S}_i \cdot \mathbf{S}_j - \frac{1}{2}\sum_{\langle ij\rangle\perp} J_c^{\text{aniso}} \mathrm{S}_i^z \mathrm{S}_j^z - D\sum_i (\mathrm{S}_i^z)^2 - \sum_i \mu_s \mathbf{B}\cdot\mathbf{S}_i \quad (1)$$

where *i* labels the Mn ions, $\mathbf{S}_i$ are unit vectors, J_{ij} are the pairwise intralayer exchange interactions, J_c is the nearest-neighbor interlayer exchange, J_c^{aniso} is the nearest-neighbor interlayer anisotropic two-ion exchange, D is the single-ion uniaxial anisotropy energy, $\mu_s = 5\mu_B$ is the size of the Mn magnetic moment in Bohr magnetons and **B** is the externally applied magnetic field in Tesla. The magnon-band dispersions in the ordered magnetic phases are calculated by solving the Landau-Lifshitz-Gilbert equation and calculating the spin-spin correlation functions in frequency and reciprocal space. The value of all parameters and the methods are detailed in the Supplementary Materials.

Figure 2 shows the calculated magnon-band dispersions. For reference, the dashed lines qualitatively depict the lowest velocity, in-plane acoustic branch of the phonon dispersion of $MnBi_2Te_4$ based on the monolayer phonon dispersion [5], dispersing from 0 to 5 meV from the zone center to the edge. Our experiment data was measured from 3 K to 25 K, corresponding to a k_BT scale of 0.25-2.15 meV.

In zero magnetic field, the system is in the AFM phase and the magnons have a near linear dispersion (Fig. 2(a)). There are two modes with opposite magnon spin polarization, but in zero field these are degenerate. A 0.6 meV gap at the zone center is induced by the magnetic anisotropy, enhanced by the exchange energy in antiferromagnets. An external magnetic field along *z* breaks the symmetry between the spin-up and spin-down moments, thus lifting the degeneracy of the AFM magnon branches into two bands with a gap proportional to the external field strength (Fig. 2b-d). Increasing the magnetic field blueshifts one branch and redshifts the other. The redshifted branch becomes the dominant scatterer since the thermal magnon density increases as the band moves to lower energies whereas the magnon occupation of the high-energy branch decreases. Once the lower magnon mode has closed the energy gap at the zone center, further increasing the applied magnetic field causes an instability in the magnetic order, producing the spin-flop transition and the CAFM phase (Fig. 2(e)). In the CAFM phase, there is a gapless magnon branch attributed to a Goldstone mode and another high-energy branch. The gapless mode retains its dispersion throughout the CAFM regime without a dependence on the magnetic field. Above a critical field, the magnetic moments are forced to align with the magnetic field, and the FM phase is established with the upper branch being the ferromagnetic-like branch and lower being of an antiferromagnetic branch with zero magnetization (Fig. 2(f-h)) [35]. The magnetic field increases the energy of both modes, opening a gap in the zone center proportional to the Zeeman energy, $g\mu_B B_z$.

The trends of κ_{xx} (B_z) can not be explained by magnon thermal conductivity based on the calculated magnon spectrum. The magnon gap closed by the field in the CAFM phase would result in a higher magnon density, thus increasing heat carrier density. Given the similar dispersion, magnon thermal conductivity would increase in the CAFM phase. This contrasts with the data presented in which κ_{xx} approaches a minimum as the gap is closed, stays at the minimum when the gap is zero throughout CAFM phase and increases as the gap opens again.

To understand the changes in thermal conductivity in the different magnetic phases we consider the relationship between the magnon spectrum and the acoustic phonon dispersion. To first order, the dominant magnon-phonon interactions can be broken down into three classes: hybridization at crossing points of the dispersion, the magnon-number non-conserving confluence process, and magnon-number-conserving Cherenkov scattering [12].

Magnon-phonon hybridization can occur at the touching points between magnon and phonon dispersions. The strength of magnon-phonon hybridization depends on the volume of the phase space at the touching point [13]. In all cases here the bands simply cross and so the hybridization is likely to be weak. In the CAFM phase, there is no magnon gap for the lower branch; thus, hybridization cannot happen on the lower branch, yet the thermal conductivity forms a minimum in this regime, suggesting hybridization is not the dominant mechanism to explain the data. From the neutron scattering data [34], the hybridization was also not observed; again, suggesting that it is a weak effect.

Cherenkov scattering, which conserves the magnon number, can be expected in all magnetic phases. This process involves a magnon scattering into a phonon and a lower energy magnon. The scattering rate for this process depends on the detailed shape of the magnon dispersion but is allowed by energy and momentum conservation throughout the Brillouin zone. The scattering cross section will have some field dependence as the magnon dispersion changes with field, but no angular momentum is transferred to the lattice and both total energy and total linear momentum of the two magnons and one phonon are conserved; thus it cannot alter the thermal transport. Finally, we suggest that the magnon-number non-conserving confluence processes where both energy and angular momentum is transferred is the most relevant process in explaining our data. In this process, two magnons interact with a phonon. The process must obey the conservation of energy and angular momentum $\epsilon_{\mathbf{k}} + \epsilon_{\mathbf{k}'} - \omega_{\mathbf{q}\lambda} = 0$, where $\epsilon_{\mathbf{k}}$ is a magnon dispersion and $\omega_{\mathbf{q}\lambda}$ is the phonon dispersion with polarization λ. Crucially, *this process is forbidden for phonons at energies less than twice the size of the magnon gap*. These low energy phonons, corresponding to long wavelengths, typically can travel long distances across the lattice without scattering. They also have a very large thermal population according to Bose-Einstein statistics. Thus, they are the dominant heat-carrying phonons. As the magnon gap closes to zero in the CAFM phase, the confluence process is allowed everywhere in the Brillouin zone and interactions between magnons and the dominant heat-carrying phonons can occur. The zero gap in the CAFM phase also leads to a higher magnon density. In the end, two factors work together to explain the flat and lower thermal conductivity data in the CAFM phase: lower momentum phonons being scattered, and higher magnon density causing more scattering. These two factors have the opposite field dependence in the AFM and FM phases. In the AFM phase, the forbidden region becomes smaller with field, while in the FM phase, the forbidden region expands with field. This explains the opposite field dependence of thermal conductivity in these two phases. In Fig. 1(a), we notice that the magnetic field dependence $d\kappa_{xx} / dB_z$ becomes larger in both AFM and FM phases as the temperature decreases. This behavior can be explained in term of the smearing of the forbidden gap at finite temperature.

Thermal Hall effect

Thermal Hall effect can arise as a result of magnon-phonon interactions in antiferromagnets, as suggested by some theoretical studies. If the magnon-phonon interaction is strong, anti-crossing points at magnon-phonon hybridization can generate hotspots of Berry curvature and thermal Hall effe [14] ct [14]. In an out-of-plane external magnetic field, both antiferromagnets [15] and ferromagnets [16] may have magnon-polaron bands that can carry Chern number, even though the individual magnon and phonon bands are topologically trivial by themselves. This could give rise to a phonon Hall effect. Our magnon band calculation shows that there is a possibility that magnon-phonon hybridization can occur in $MnBi_2Te_4$. However, this effect is not seen in neutron scattering data [34]. The thermal Hall effect, in the form of magnetic field dependence of κ_{xy}, was measured and is shown in Fig. 3(a). Above T_N, κ_{xy} is a linear function of the field up to 9 T with the slope $d\kappa_{xy}/dB_z$ decreasing as the temperature decreases. Below T_N, the absolute value of κ_{xy} shows an abrupt increase at the spin-flop transition with increasing field. κ_{xy}, is congruent with the electrical Hall resistivity (see Supplementary Materials and Ref. [36]). In Fig. 3(b), we show the calculated $\kappa_{xy,WFL} = \sigma_{xy}L_0T$ from the Wiedemann Franz law (WFL), where L_0 is the free electron value. $\sigma_{xy}L_0T$ is about half of the measured value for κ_{xy}. Figures 3(c) and (d) show raw data points and averaged curves at T=10.6 K and 15.3 K, respectively. A drop in κ_{xy} at 3.5 T is observed, coinciding with the spin-flop transition, and we attribute it to the anomalous thermal Hall effect. The close agreement within an order of magnitude indicates that the majority of thermal Hall conductivity is electronic in origin and is from the bulk. However, it is unexpected that the measured κ_{xy}, is much larger than the estimated value using WFL, i.e., $\kappa_{xy} > \sigma_{xy}L_0T$. If κ_{xy} is purely electronic and the Lorenz number is identical to the free electron value, κ_{xy} is shorted by the lattice thermal conductivity, and we would expect $\kappa_{xy} < \sigma_{xy}L_0T$. The WFL with the free electron Lorenz ratio strictly only holds for elastic diffuse scattering. It is therefore not a priori for thermal transport in magnetic field or in the anomalous case of a magnetic material. In this case, it could be attributed to either a doubling of the Lorenz ratio over the free electron value, or to a magnon contribution, or to a chiral phonon effect either due to skewed magnetic scattering [37] or magnon-polaron bands [13–20]. If there is a phonon Hall effect, it would also be visible at the CAFM to FM yet we do not see evidence for this. Perhaps, the effect is too small compared to the electronic signal. Revisiting the interpretation of the κ_{xy} data and neutron scattering data [34], we conclude that there is no evidence of magnon phonon hybridization but the main interaction between magnon and phonon in MBT is a scattering effect, which we explained, controlled by the magnon band gap.

Conclusion

In summary, we show that $MnBi_2Te_4$ exhibits a significant and complex field-dependent magneto-thermal conductivity. We elucidate the mechanism to be one where phonons carry the heat and are subjected to magnetic scattering. More specifically, the two magnon scatter one phonon process is likely the dominant interaction that affects thermal transport in MBT in an out-of-plane magnetic field. Magnon-phonon interactions can induce an important field dependence to the amount of heat carried by the lattice, potentially opening a new mechanism to realize heat switches, an enabling technology for solid-state heat engines and controlled cooling technologies.

References

[1] D. Vu, W. Zhang, C. Şahin, M. E. Flatté, N. Trivedi, and J. P. Heremans, *Thermal Chiral Anomaly in the Magnetic-Field-Induced Ideal Weyl Phase of Bi1−xSbx*, Nature Materials 2021 20:11 **20**, 1525 (2021).

[2] P. M. Sass, J. Kim, D. Vanderbilt, J. Yan, and W. Wu, *Robust A-Type Order and Spin-Flop Transition on the Surface of the Antiferromagnetic Topological Insulator MnBi2Te4*, Phys Rev Lett **125**, 037201 (2020).

[3] S.-K. Bac et al., *Topological Response of the Anomalous Hall Effect in MnBi2Te4 Due to Magnetic Canting*, NPJ Quantum Mater **7**, 46 (2022).

[4] M. M. Otrokov et al., *Prediction and Observation of an Antiferromagnetic Topological Insulator*, Nature **576**, 416 (2019).

[5] J. Li, Y. Li, S. Du, Z. Wang, B. L. Gu, S. C. Zhang, K. He, W. Duan, and Y. Xu, *Intrinsic Magnetic Topological Insulators in van Der Waals Layered MnBi2Te4-Family Materials*, Sci Adv **5**, (2019).

[6] D. Zhang, M. Shi, T. Zhu, D. Xing, H. Zhang, and J. Wang, *Topological Axion States in the Magnetic Insulator MnBi2Te4 with the Quantized Magnetoelectric Effect*, Phys Rev Lett **122**, (2019).

[7] C. Lei, S. Chen, and A. H. MacDonald, *Magnetized Topological Insulator Multilayers*, Proc Natl Acad Sci U S A **117**, 27224 (2020).

[8] H. Padmanabhan et al., *Interlayer Magnetophononic Coupling in MnBi2Te4*, Nature Communications 2022 13:1 **13**, 1 (2022).

[9] J. Choe et al., *Electron-Phonon and Spin-Lattice Coupling in Atomically Thin Layers of MnBi2Te4*, Nano Lett **21**, 6139 (2021).

[10] H. Zhang, C. Q. Xu, S. H. Lee, Z. Q. Mao, and X. Ke, *Thermal and Thermoelectric Properties of an Antiferromagnetic Topological Insulator MnBi2Te4*, Phys Rev B **105**, 184411 (2022).

[11] R. A. Robinson, S. H. Lee, L. Min, J. Ning, J. Sun, and Z. Mao, *Evidence of Weyl Fermion Enhanced Thermal Conductivity Under Magnetic Fields in Antiferromagnetic Topological Insulator Mn(Bi(1-x)Sb(x))2Te4*, (2023).

[12] A. Rückriegel, S. Streib, G. E. W. Bauer, and R. A. Duine, *Angular Momentum Conservation and Phonon Spin in Magnetic Insulators*, Phys Rev B **101**, (2020).

[13] T. Kikkawa, K. Shen, B. Flebus, R. A. Duine, K. I. Uchida, Z. Qiu, G. E. W. Bauer, and E. Saitoh, *Magnon Polarons in the Spin Seebeck Effect*, Phys Rev Lett **117**, 207203 (2016).

[14] X. Zhang, Y. Zhang, S. Okamoto, and D. Xiao, *Thermal Hall Effect Induced by Magnon-Phonon Interactions*, Phys Rev Lett **123**, 167202 (2019).

[15] S. Park and B. J. Yang, *Topological Magnetoelastic Excitations in Noncollinear Antiferromagnets*, Phys Rev B **99**, (2019).

[16] G. Go, S. K. Kim, and K. J. Lee, *Topological Magnon-Phonon Hybrid Excitations in Two-Dimensional Ferromagnets with Tunable Chern Numbers*, Phys Rev Lett **123**, (2019).

[17] S. Zhang, G. Go, K. J. Lee, and S. K. Kim, *SU(3) Topology of Magnon-Phonon Hybridization in 2D Antiferromagnets*, Phys Rev Lett **124**, (2020).

[18] H. Yang, X. Xu, J. H. Lee, Y. S. Oh, S. W. Cheong, and J. G. Park, *Diagonal and Off-Diagonal Thermal Conduction with Resonant Phonon Scattering in Ni3Te O6*, Phys Rev B **106**, 144417 (2022).
[19] T. Ideue, T. Kurumaji, S. Ishiwata, and Y. Tokura, *Giant Thermal Hall Effect in Multiferroics*, Nat Mater **16**, 797 (2017).
[20] H. Katsura, N. Nagaosa, and P. A. Lee, *Theory of the Thermal Hall Effect in Quantum Magnets*, Phys Rev Lett **104**, (2010).
[21] J. Q. Yan, Q. Zhang, T. Heitmann, Z. Huang, K. Y. Chen, J. G. Cheng, W. Wu, D. Vaknin, B. C. Sales, and R. J. McQueeney, *Crystal Growth and Magnetic Structure of MnBi2Te4*, Phys Rev Mater **3**, (2019).
[22] J. Q. Yan, S. Okamoto, M. A. McGuire, A. F. May, R. J. McQueeney, and B. C. Sales, *Evolution of Structural, Magnetic, and Transport Properties in MnBi2-XSbxTe4*, Phys Rev B **100**, (2019).
[23] B. Chen et al., *Intrinsic Magnetic Topological Insulator Phases in the Sb Doped MnBi2Te4 Bulks and Thin Flakes*, Nature Communications 2019 10:1 **10**, 1 (2019).
[24] M. H. Du, J. Yan, V. R. Cooper, and M. Eisenbach, *Tuning Fermi Levels in Intrinsic Antiferromagnetic Topological Insulators MnBi2Te4 and MnBi4Te7 by Defect Engineering and Chemical Doping*, Adv Funct Mater **31**, (2021).
[25] F. Hou et al., *Te-Vacancy-Induced Surface Collapse and Reconstruction in Antiferromagnetic Topological Insulator MnBi2Te4*, ACS Nano **14**, 11262 (2020).
[26] J. P. Heremans, R. J. Cava, and N. Samarth, *Tetradymites as Thermoelectrics and Topological Insulators*, Nature Reviews Materials.
[27] S. R. Boona and J. P. Heremans, *Magnon Thermal Mean Free Path in Yttrium Iron Garnet*, Phys Rev B Condens Matter Mater Phys **90**, (2014).
[28] G. A. Slack, *Thermal Conductivity of CaF2, MnF2, CoF2, and ZnF2 Crystals*, Physical Review **122**, 1451 (1961).
[29] G. A. Slack and R. Newman, *Thermal Conductivity of MnO and NiO*, Phys Rev Lett **1**, 359 (1958).
[30] C. Kittel, *Interaction of Spin Waves and Ultrasonic Waves in Ferromagnetic Crystals*, Physical Review **110**, 836 (1958).
[31] A. Zeugner et al., *Chemical Aspects of the Candidate Antiferromagnetic Topological Insulator MnBi2Te4*, Chemistry of Materials **31**, 2795 (2019).
[32] X. Hong et al., *Strongly Scattered Phonon Heat Transport of the Candidate Kitaev Material Na2Co2TeO6*, Phys Rev B **104**, (2021).
[33] T. M. McCormick, S. J. Watzman, J. P. Heremans, and N. Trivedi, *Fermi Arc Mediated Entropy Transport in Topological Semimetals*, Phys Rev B **97**, 195152 (2018).
[34] B. Li, D. M. Pajerowski, S. X. M. Riberolles, L. Ke, J. Q. Yan, and R. J. McQueeney, *Quasi-Two-Dimensional Ferromagnetism and Anisotropic Interlayer Couplings in the Magnetic Topological Insulator MnBi2Te4*, Phys Rev B **104**, L220402 (2021).
[35] A. G. Gurevich and G. A. Melkov, *Magnetization Oscillations and Waves*, Magnetization Oscillations and Waves (1996).
[36] S. H. Lee et al., *Spin Scattering and Noncollinear Spin Structure-Induced Intrinsic Anomalous Hall Effect in Antiferromagnetic Topological Insulator MnBi2Te4*, Phys Rev Res **1**, (2019).

[37] B. Flebus and A. H. Macdonald, *Charged Defects and Phonon Hall Effects in Ionic Crystals*, Phys Rev B **105**, (2022).

Acknowledgments

We thank Dr. Brian Skinner for the helpful discussions. Simulations in this work were undertaken on ARC4, part of the High Performance Computing facilities at the University of Leeds, UK.

Funding:

US Office of Naval Research MURI "Extraordinary electronic switching of thermal transport" grant # N00014-21-1-2377 (RAN, JEG, JPH).\

US Department of Defense SMART fellowship (BLW)

US National Science Foundation MRSEC "Center for Emerging Materials", grant # DMR 201 1876 (DDV)

Royal Society University Research Fellowship URF\R1\180333 (JB).

Author contributions:

The samples were synthesized by RAN and JEG; the experiments were designed and carried out by DDV and BLW under supervision of JPH; the integration between theory and experiment was done by DDV, JB and JPH, the magnon spectrum calculations by JB. All authors contributed to data analysis and writing the manuscript.

Competing interests:

The authors declare no competing financial interests.

Data and materials availability:

The datasets generated and/or analyzed during the current study are available from the corresponding author on reasonable request.

Tables and Figures

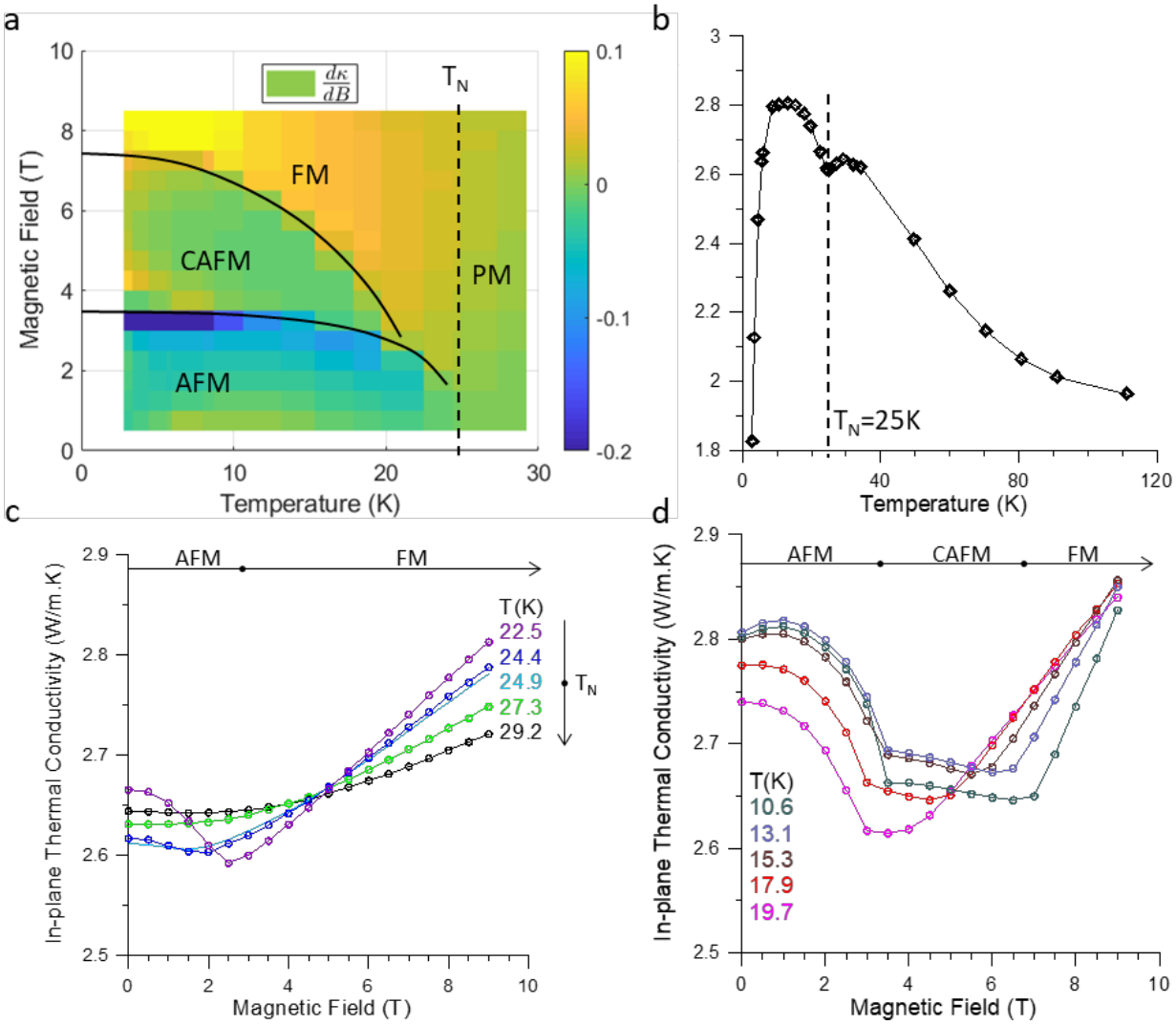

Fig. 1. (a) The magnetic ordering phase diagram, full lines from the literature [2,3]. The color map is reconstructed by taking the field derivatives $d\kappa_{xx}/dB$ of the following frames. The large negative value near the boundary of AFM phase corresponds to the spin-flop transition. (b) Temperature dependence of total in-plane thermal conductivity κ_{xx}. κ_{xx} decreases at the ordering temperature T_N=24.5K indicating scattering of phonon to magnon. (c, d) Field dependence of in-plane thermal conductivity $\kappa_{xx}(B_z)$. Across the ordering temperature, $\kappa_{xx}(B_z)$ develops contrasting behavior at different field ranges. Above T_N, κ_{xx} plateaus at low field then slightly increases with field. Below T_N, κ_{xx} decreases with field at low field and increases linearly in field at high field. The magnetic field at which the field dependence changes correspond to the transition from AFM to FM ordering. Below 20 K, in addition to the initial decrease in AFM phase and linear increase in FM phase, there is a plateau in the magnetic field range corresponding to the Canted AFM ordering phase.

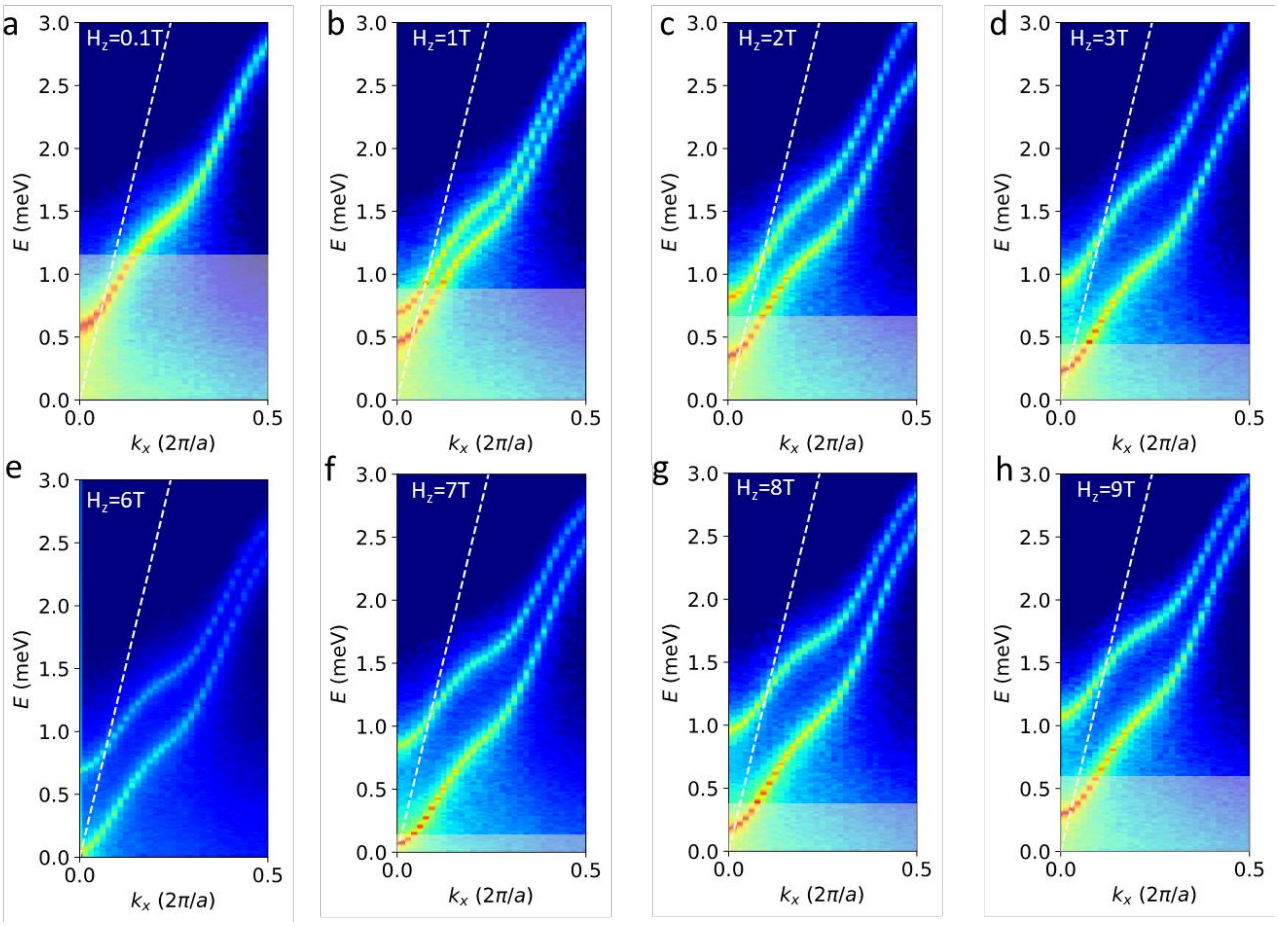

Fig. 2. Calculated magnon band evolution in an out-of-plane magnetic field. (a-d) magnon bands in the AFM ordering phase (e) magnon bands in the canted AFM ordering phase and (f-h) magnon bands in FM ordering phase. The dashed lines qualitatively depict the lowest velocity, in-plane longitudinal acoustic branch of the phonon dispersion of $MnBi_2Te_4$ based on the monolayer phonon dispersion [5]. The light-shaded regions mark the forbidden region for magnon number non-conserving confluence process.

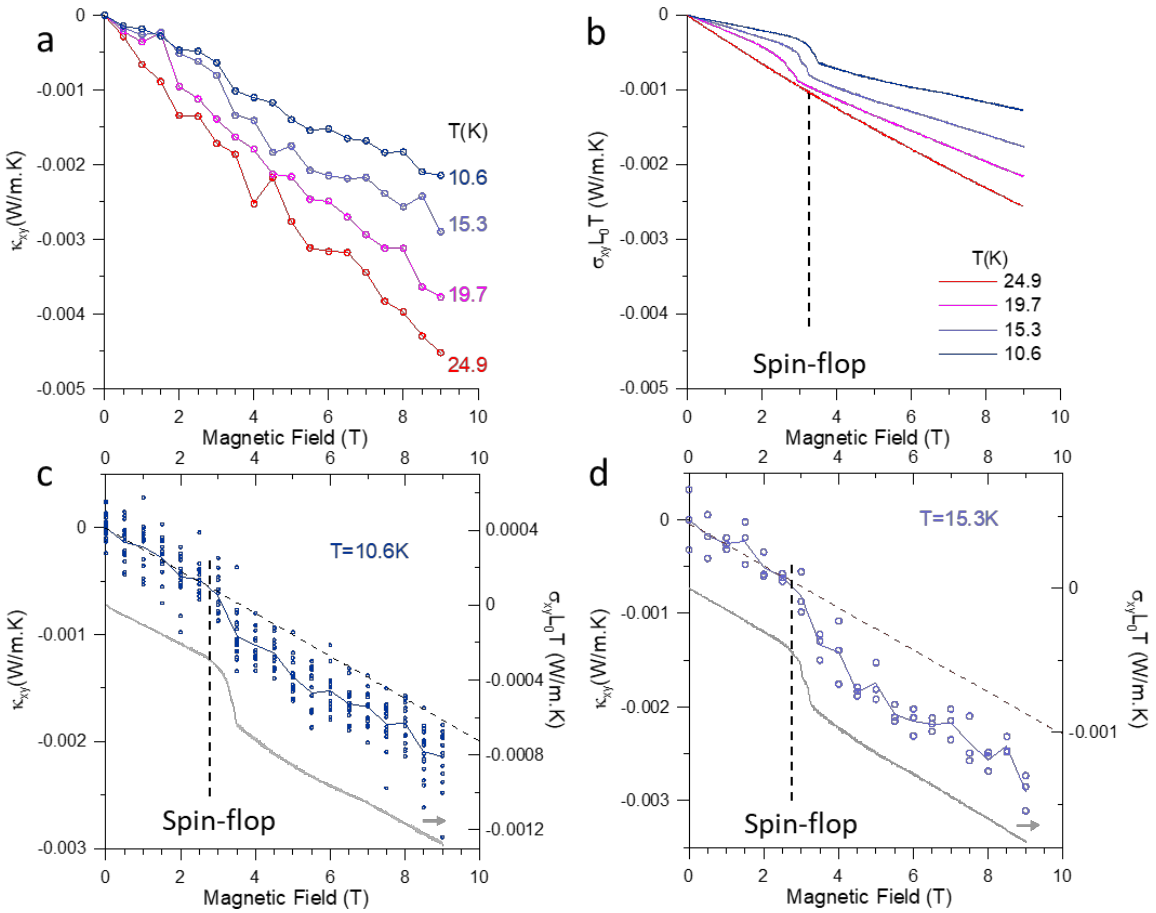

Fig. 3. Thermal Hall conductivity and comparison with Wiedemann Franz Law. (a) Thermal Hall conductivity κ_{xy} verses applied magnetic fields measured below T_N. (b) Thermal Hall conductivity calculated from Wiedemann Franz Law $\kappa_{xy} = \sigma_{xy} L_0 T$ at corresponding temperatures. Quantitatively, measured thermal Hall conductivity is approximately twice as large as values predicted by Wiedemann Franz Law. (c, d) Blown-up plots of κ_{xy} data at 15.3 K and 10.6 K shows an anomalous thermal Hall effect with a distinctive jump at the spin-flop transition. Individual data points are shown along with the lines connecting their mean values at each magnetic field. Dashed lines are linear fit drawn through the low field data points in the CAFM phase. The axes on the right shows corresponding thermal Hall conductivity calculated using WFL and electrical conductivity for comparison.

Supplemental Material for Magnetic field-controlled lattice thermal conductivity in $MnBi_2Te_4$

Dung D. Vu
Department of Mechanical and Aerospace Engineering, The Ohio State University, USA

Ryan A. Nelson and Joshua E. Goldberger
Department of Chemistry and Biochemistry, The Ohio State University, Columbus, USA

Brandi L. Wooten
Department of Materials Science and Engineering, The Ohio State University, Columbus, USA

Joseph Barker
School of Physics and Astronomy, University of Leeds, United Kingdom

Joseph P. Heremans*
Department of Mechanical and Aerospace Engineering, The Ohio State University, Columbus, USA
Department of Materials Science and Engineering, The Ohio State University, Columbus, USA and
Department of Physics, The Ohio State University, Columbus, USA

* Corresponding author (Email: heremans.1@osu.edu)

I. ATOMISTIC SPIN DYNAMICS

A. Methods

$MnBi_2Te_4$ belongs to the $R\bar{3}m$ (166) space group. We performed calculations using the magnetic primitive cell which has the basis vectors

$$\begin{aligned}\mathbf{a} &= a(\quad 0.500000, \quad 0.288675, \quad 6.293360)\\ \mathbf{b} &= a(-0.500000, \quad 0.288675, \quad 6.293360)\\ \mathbf{c} &= a(\quad 0.000000, -0.577350, \quad 6.293360)\end{aligned} \tag{S1}$$

with the lattice constant $a = 4.3337$ Å. In the primitive cell, there are only two Mn atoms, one of each of the antiferromagnetic sublattices. In fractional coordinates, these are located at

$$\begin{aligned}\mathrm{Mn_A} &= (0.0, 0.0, 0.0)\\ \mathrm{Mn_B} &= (0.5, 0.5, 0.5).\end{aligned} \tag{S2}$$

We use the Hamiltonian and parameters for $MnBi_2Te_4$ suggested in Ref. S1 on the basis of linear spin wave theory fitting of inelastic neutron scattering measurements. The Hamiltonian written in our conventions is

$$\begin{aligned}\mathcal{H} = &-\frac{1}{2}\sum_{\langle ij\rangle_\parallel} J_{ij}\mathbf{S}_i\cdot\mathbf{S}_j - \frac{1}{2}\sum_{\langle ij\rangle_\perp} J_c\mathbf{S}_i\cdot\mathbf{S}_j\\ &-\frac{1}{2}\sum_{\langle ij\rangle_\perp} J_c^{\mathrm{aniso}} S_i^z\cdot S_j^z - D\sum_i (S_i^z)^2 - \sum_i \mu_s\mathbf{B}\cdot\mathbf{S}_i\end{aligned} \tag{S3}$$

where factors of $1/2$ are for the double counting in the sum and $\mathbf{S}_i$ are unit vectors. J_{ij} are the isotropic intraplane exchange energies, J_c is the isotropic interplane exchange energy, J_c^{aniso} is the anisotropic interplane exchange energy, D is a single-ion uniaxial anisotropy, μ_s is the size of the magnetic moment and $\mathbf{B}$ is an externally applied magnetic field in Tesla. $\langle\cdots\rangle$ indicates that a sum is performed only over a limited number of neighbours and $\parallel$ denotes inp-lane and $\perp$ out-of-plane neighbours. The parameters values and units are given in tables S1 and S2.

We solve the spin dynamics using the Landau-Lifshitz equation

$$\frac{\mathrm{d}\mathbf{S}_i}{\mathrm{d}t} = -\gamma\left[\mathbf{S}_i\times\mathbf{H}_i + \alpha\mathbf{S}_i\times(\mathbf{S}_i\times\mathbf{H}_i)\right], \tag{S4}$$

TABLE S1. Exchange constants for the Hamiltonian (S3). $J_\parallel$ are intra-plane and J_c are interplane interactions. A single interaction vector is given in fractional coordinates; equivalent vectors can be generated from the R$\bar{3}$m space group operations. The interaction distances are given in units of the lattice constant (a).

symbol	vector (fractional coordinates)	number	distance (lattice constants)	value (meV)
$J_{\parallel 1}$	$(\ 1,\ 0,-1)$	6	1.000000	0.5825
$J_{\parallel 2}$	$(\ 1,\ 1,-2)$	6	1.732051	-0.0825
$J_{\parallel 3}$	$(\ 0,\ 2,-2)$	6	2.000000	0.0175
$J_{\parallel 4}$	$(\ 1,\ 2,-3)$	12	2.645751	-0.0075
$J_{\parallel 5}$	$(\ 0,\ 0,\ 3)$	6	3.000000	0.0400
$J_{\parallel 6}$	$(\ 0,\ 2,\ 2)$	6	3.464102	0.0325
$J_{\parallel 7}$	$(\ 0,\ 1,\ 3)$	12	3.605551	0.0200
J_c	$(\ \frac{1}{2},\ \frac{1}{2},-\frac{1}{2})$	6	3.199207	-0.1625
J_c^{aniso}	$(\ \frac{1}{2},\ \frac{1}{2},-\frac{1}{2})$	6	3.199207	-0.0575

TABLE S2. Model parameters used in the Hamiltonian (S3) and Landau-Lifshitz equation (S4).

Symbol	Value
D	0.2035 meV
μ_s	$5\mu_B$
α	0.05
γ	$1.76 \times 10^{11}\text{rad}\,\text{s}^{-1}\text{T}^{-1}$

where γ is the gyromagnetic ratio and α is a damping parameter with the values given in Table S2. The effective field $\mathbf{H}_i$ on each lattice site is

$$\mathbf{H}_i = -\frac{1}{\mu_s}\frac{\partial \mathcal{H}}{\partial \mathbf{S}_i} + \boldsymbol{\xi}_i \tag{S5}$$

with $\boldsymbol{\xi}_i$ being a vector of stochastic processes that provide thermal fluctuations. The temperature is introduced through a quantum thermostat that obeys the quantum fluctuation dissipation theorem [S2] with the statistical properties of ξ_i defined as

$$\langle \xi_{a,i}(t) \rangle = 0;\ \langle \xi_{a,i}\xi_{b,j} \rangle_\omega = \delta_{ij}\delta_{ab}\frac{2\alpha}{\gamma\mu\beta}\frac{\hbar\omega}{\mathrm{e}^{\beta\hbar\omega}-1}, \tag{S6}$$

where a and b are Cartesian components, ω is the frequency, $\beta = (k_\text{B}T)^{-1}$ is the inverse thermal energy with k_B is the Boltzmann constant and T is the temperature, $\hbar$ is Dirac's constant, $\langle \cdots \rangle$ is a statistical time average and $\langle \cdots \rangle_\omega$ is a statistical average in frequency space. The stochastic process which produces this coloured noise is generated by solving a set of second-order stochastic partial differential equations (see refs. S2 and S3 for details). These equations and the Landau-Lifshitz equation are numerically integrated with a fourth-order Runge-Kutta integration scheme with a timestep $\Delta t = 1$ fs.

The noise introduced by the thermostat induces spin fluctuations which result in a thermal distribution of magnons within the spectrum. The use of a quantum thermostat ensures that the magnons have a Planck distribution.

B. Validation of model parameters

In Ref. S1 the spin vectors have length $S = 5/2$ but in our model the spin vectors are of unit length and the size of the spin moment appears in the parameter μ_s. Therefore, our exchange interactions are $J_{ij}^{\text{this work}} = SJ_{ij}^{\text{Li et al.}}$. The double counting convention and the exact definition of $\langle ij \rangle$ in Ref. S1 are unclear. Therefore, we calculated the neutron scattering cross section within our code (Fig. S1 and compared it with their experimental and simulated spectra to ensure that our models are equivalent.

Our neutron scattering cross section is calculated from

$$\begin{aligned}\mathcal{S}(\mathbf{Q},\omega) = &\frac{g_n^2 r_c^2}{2\pi\hbar}\sum_{ab}\left(\delta_{ab} - \hat{Q}_a\hat{Q}_b\right) \\ &\times \sum_{d,d'}\mathrm{e}^{-i\mathbf{Q}\cdot(\mathbf{r}_d-\mathbf{r}_{d'})}\sum_{l,l'}\mathrm{e}^{-i\mathbf{Q}\cdot(\mathbf{R}_l-\mathbf{R}_{l'})} \\ &\times \int_{-\infty}^{\infty} e^{-i\omega t}\left[\left\langle S_{ld}^a(0)S_{l'd'}^b(t)\right\rangle - \left\langle S_{ld}^a\right\rangle\left\langle S_{l'd'}^b\right\rangle\right]dt,\end{aligned} \tag{S7}$$

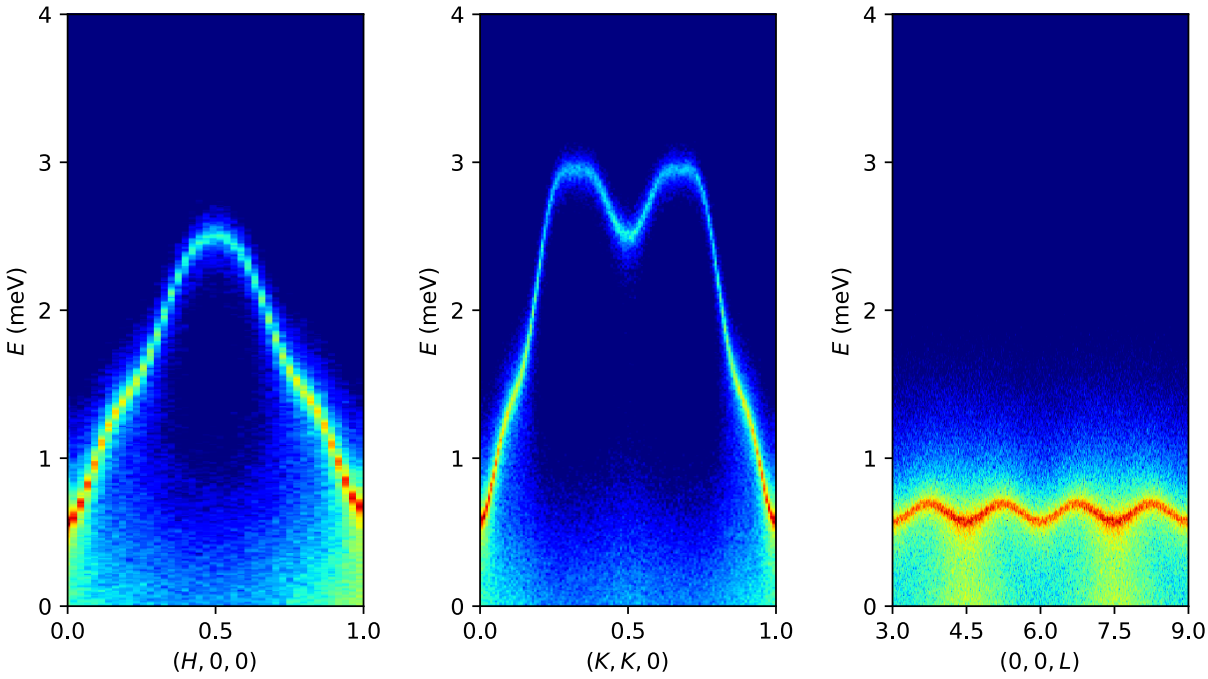

FIG. S1. $MnBi_2Te_4$ neutron scattering cross sections at $T = 2$ K and $B_z = 0.1$ T to compare with Ref. S1 Fig. 2

where $a, b = \{x, y, z\}$ are Cartesian components, $\mathbf{R}_l$ is the position of the l-th unit cell, $\mathbf{r}_d$ is the d-th position in the unit cell, $g_n = 1.931$ is the neutron g-factor, $r_c = e^2/m_e c^2 = 2.8$ fm is the classical electron radius with e, m_e, and c the elementary charge, the mass of the electron and the speed of light, $\mathbf{Q}$ is the scattering vector and $\hat{\mathbf{Q}} = \mathbf{Q}/|\mathbf{Q}|$. δ_{ab} is the Kronecker delta function. $\mathcal{S}(\mathbf{Q}, E) = \mathcal{S}(\mathbf{Q}, \hbar\omega)$.

C. Magnon Spectrum Calculation

Simulations calculating the neutron scattering cross section using (S7) are useful to compare with neutron scattering experiments. However, the results obscure the details of the underlying theoretical magnon spectrum due to the projection onto the scattering vector $(\delta_{ab} - \hat{Q}_a \hat{Q}_b)$ and the effect of the structure factor.

We calculate the theoretical magnon spectrum in a reduced-zone scheme so that it contains all bands. This is essentially the dynamical structure factor where the spins have been transformed so that we study their fluctuations around a common reference state.

We first apply a rotation, $\mathbb{W}_d$, to each spin position d of the unit cell:

$$\tilde{\mathbf{S}}_d = \mathbb{W}_d \cdot \mathbf{S}_d \tag{S8}$$

such that the spin is rotated to align with the z-axis and the oscillations of the spin are about this axis. We then calculate the total dynamical structure factor as

$$\begin{aligned}\mathcal{W}_{ab}(\mathbf{k}, \omega) = \frac{1}{2\pi} \sum_d \mathrm{e}^{-i\mathbf{k}\cdot\mathbf{r}_d} \sum_{l,l'} \mathrm{e}^{-i\mathbf{k}\cdot(\mathbf{R}_l - \mathbf{R}_{l'})} \\ \times \int_{-\infty}^{\infty} e^{-i\omega t} \left[\left\langle \tilde{S}^a_{ld}(0) \tilde{S}^b_{l'd'}(t) \right\rangle - \left\langle \tilde{S}^a_{ld} \right\rangle \left\langle \tilde{S}^b_{l'd'} \right\rangle \right] dt.\end{aligned} \tag{S9}$$

where $\mathbf{k}$ is a reciprocal space vector in the first Brillouin zone. To produce the figures in the main text, we plot the transverse components of the dynamical structure factor $(\mathcal{W}_{xx}(\mathbf{k}, \omega) + \mathcal{W}_{yy}(\mathbf{k}, \omega))^{1/2}$.

The resulting figures contain all bands in the magnon spectrum, and the intensity reflect their thermal occupation.

[S1] B. Li, D. M. Pajerowski, S. X. M. Riberolles, L. Ke, J.-Q. Yan, and R. J. McQueeney, Quasi-two-dimensional ferromagnetism and anisotropic interlayer couplings in the magnetic topological insulator $MnBi_2Te_4$, Phys. Rev. B **104**, L220402 (2021).
[S2] J. Barker and G. E. W. Bauer, Semiquantum thermodynamics of complex ferrimagnets, Phys. Rev. B **100**, 140401(R) (2019).
[S3] A. V. Savin, Y. A. Kosevich, and A. Cantarero, Semiquantum molecular dynamics simulation of thermal properties and heat transport in low-dimensional nanostructures, Phys. Rev. B **86**, 064305 (2012).

II. SUPPLEMENTAL DATA

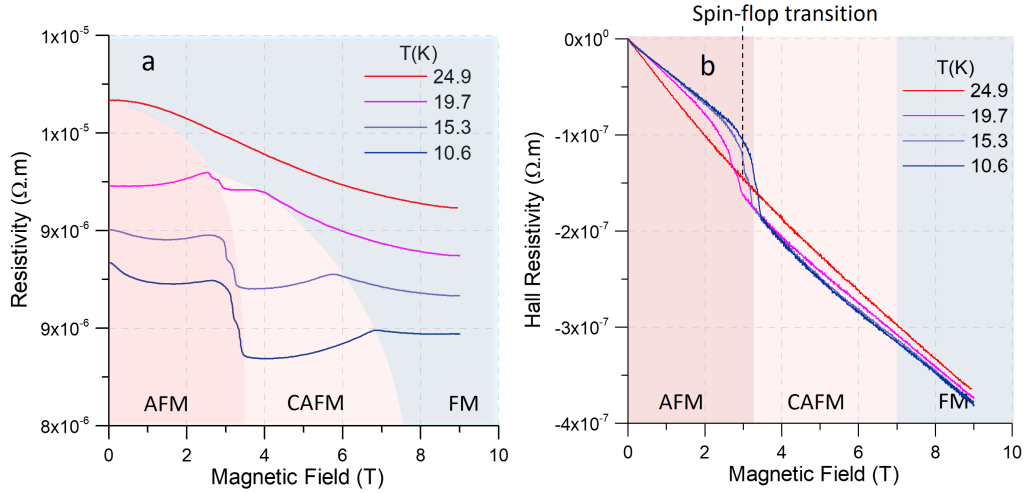

FIG. S2. Resistivity and Hall resistivity data. (a) Field dependence of in-plane resistivity $\rho_{xx}(B_z)$. At Spin flop transition, the resistivity drop, attributed to spin valve effect. (b) Hall resistivity $\rho_{xy}(B_z)$ shows anomalous Hall effect at the spin-flop transition.

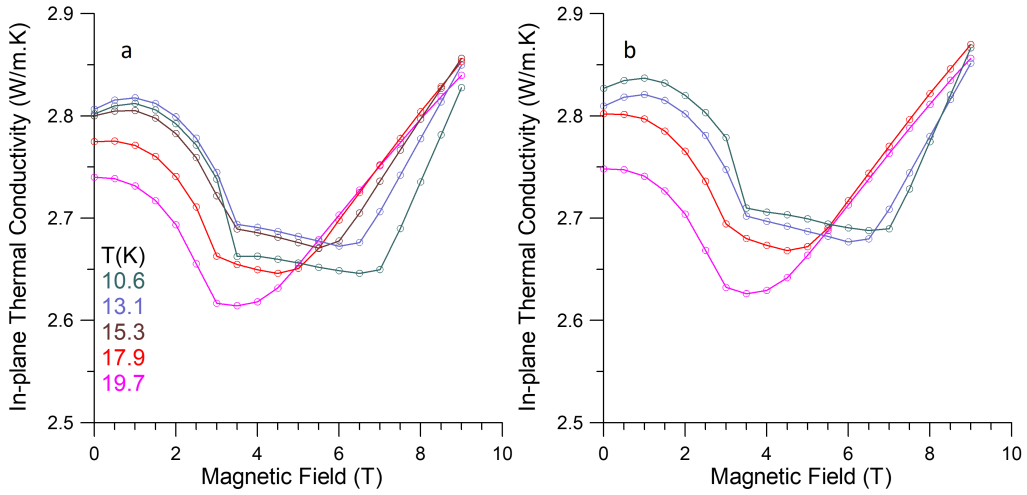

FIG. S3. Experimental test for presence of Fermi arc thermal transport. (a) In-plane thermal conductivity $\kappa_{xx}(B_z)$ with B in the out-of-plane direction (b) In-plane thermal conductivity $\kappa_{xx}(B_z)$ with B 10° intentionally misaligned from the the out-of-plane direction shows no change of slope in the FM phase.

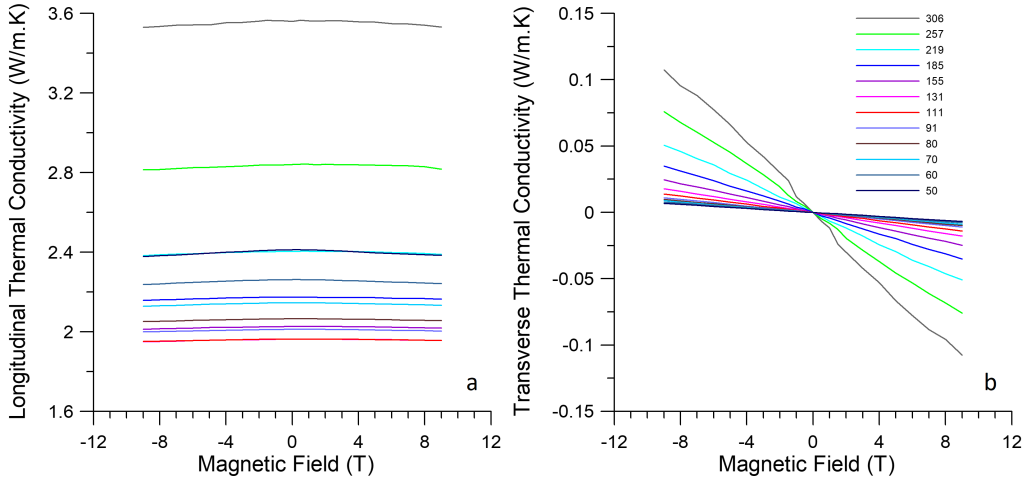

FIG. S4. Thermal conductivity data at temperatures $T \geq 50K$. (a) Longitudinal thermal conductivity $\kappa_{xx}(B_z)$, (b) Thermal Hall conductivity $\kappa_{xy}(B_z)$.

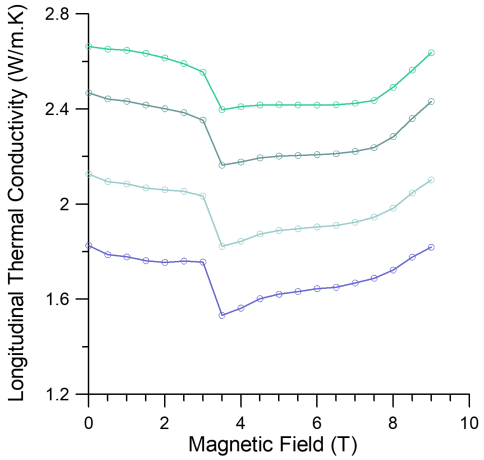

FIG. S5. Magneto thermal conductivity $\kappa_{xx}(B_z)$ data at temperatures $T \leq 6K$

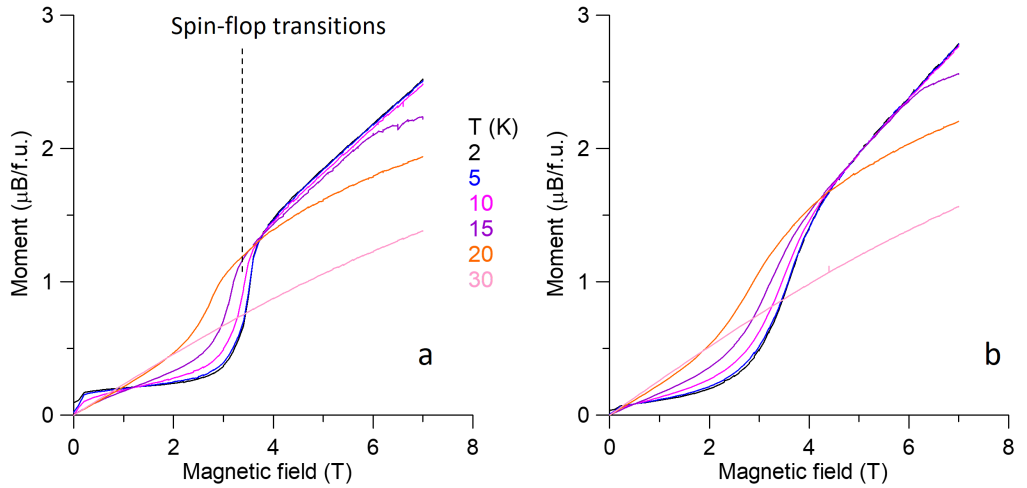

FIG. S6. Moment verses magnetic field on samples: (a) first sample with which data was reported in the main text shows sharp spin-flop transition in accordance with data reported in literature (b) second sample shows faint magnetic ordering transition and higher value of moment per formula unit, indicating the sample contains large number of free Mn atoms which act as paramagnetic free spins

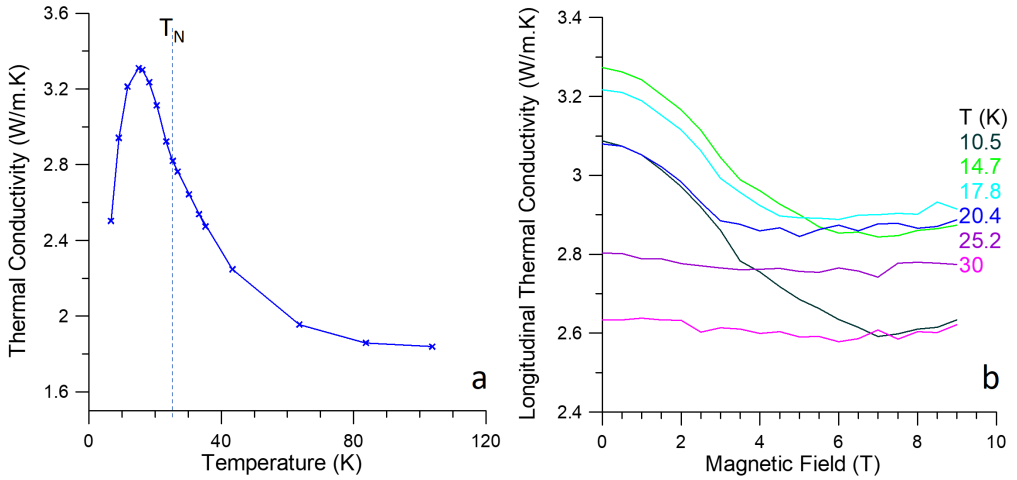

FIG. S7. Thermal conductivity and magneto thermal conductivity of second sample. (a) Thermal conductivity κ of the second sample forms higher peak in at low temperature and no visible cusp at Neel temperature suggesting smaller magnon scattering and additional contribution from paramagnetic spins in this sample. (b) Magneto thermal conductivity of the second sample at temperatures from 10 to 30 K. While this sample still shows a faint change of $d\kappa/dB$ at transitioning magnetic fields, these changes are small compared to the changes of $d\kappa/dB$ in the first sample. This is because there is an additional large decaying thermal conductivity contribution from free spins that is constrained in an applied magnetic field.

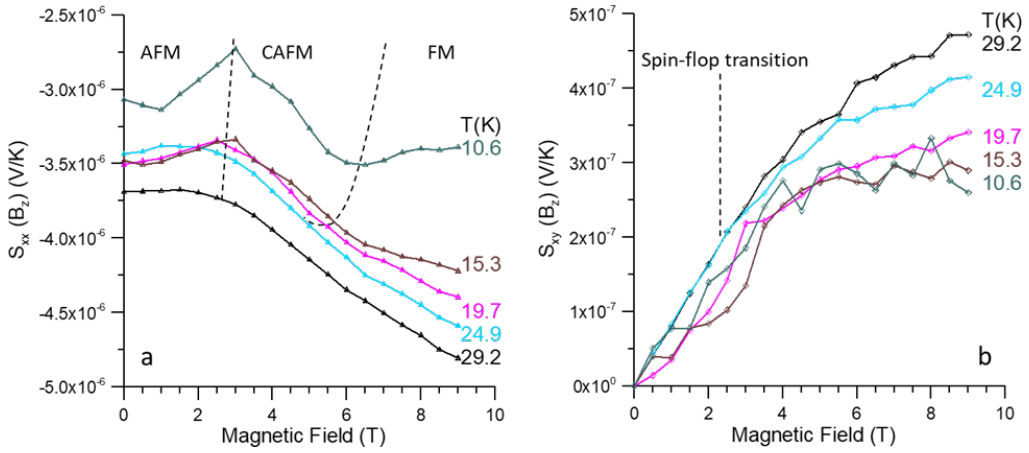

FIG. S8. Field dependence of the Seebeck $S_{xx}(B_z)$ and Nernst $S_{xy}(B_z)$ thermoelectric power. Both $S_{xx}(B_z)$ and $S_{xy}(B_z)$ are small in absolute value.(a) Below T_N, the Seebeck coefficient shows an increase with B_z in the CAFM phase and plateaus out at high field in FM phase. The small thermoelectric coefficients are consistent with a metallic system and are another result of the high Fermi level due to unintentional defect doping. In the canted AFM phase below TN, the Seebeck coefficient is slightly increased, in accordance with the slight decrease of resistivity and the Mott relation. (b)The Nernst thermopower shows a sharp change of slope at the spin-flop transition below T_N. Comparing to the magnetization data (Figure S6), the Nernst data are characteristic of the anomalous Nernst effect. Below 20 K, $S_{xy}(B_z)$ has a small slope near zero field. At the spin-flop transition, $S_{xy}(B_z)$ jumps at the same point that the magnetization changes abruptly.